Supporting Information

Conjugated Polymers with Controllable Interfacial Order and Energetics enable Tunable Heterojunctions in Organic and Colloidal Quantum Dot Photovoltaics

Yufei Zhong, Ahmad R. Kirmani, Xinzheng Lan, Joshua Carpenter, Annabel Rong-Hui Chew, Omar Awartani, Liyang Yu, Muhammad R. Niazi, Oleksandr Voznyy, Hanlin Hu, Guy Olivier Ngongang Ndjawa, Max L. Tietze, Alberto Salleo, Harald Ade, Edward H. Sargent, Aram Amassian**

Experimental details

Materials:

PBDTTT-C-T was purchased from Solarmer, PTB7 and PCE10 were purchased from 1-MATERIAL, PffBT4T-2OD and PBTTT were purchased from Ossila, P3HT (average molecular weight 50-100k, and regioregularity >90%), PCBM and PDMS (SYLGARD® 184 SILICONE ELASTOMER KIT) were purchased from Sigma. All materials are used as received.

Device fabrication:

Planar heterojuntion was fabricated by laminating polymer film atop acceptor layer, which was spin-coated onto a ZnO coated ITO substrate. ZnO layer was prepared following previous report.[1] For lamination process, polymer layer was first spin-coated onto a pre-cleaned glass substrate (with concentration of 10 mg/ml and 1500 rpm/min using CB; 10 mg/ml and 1000 rpm/min using DCB; 10 mg/ml and 4000 rpm/min using CF), resulting a film thickness of 40 nm. PCBM or acceptor layer was spin-coated onto glass/ITO/ZnO with concentration of 10 mg/ml and 1500 rpm/min using CB, giving a film thickness of 40 nm. The glass/polymer substrate was then slowly merged into water and the polymer layer was then delaminated from glass. glass/ITO/ZnO/PCBM sbustrate was used to attached to polymer layer floating on water from either top or bottom for form bilayer. For PDMS based lamination, the PDMS stamp was placed onto glass/polymer and then merged into water. The polymer film will attach to PDMS and delaminated from galss. PDMS/polymer was then placed onto accptor substrate and relased onto it. Additionally, bilayer OPV was made by thermal deposition of MoO_x/Ag (6 nm/100 nm) on top of polymer film in a vacuum thermal evaporator (3×10^{-6} mbar base pressure), using a shadow mask. The active area of the devices was 0.1 cm^2. OFET was fabricated using pre-washed Si as substrate with patterned Au atop (Fraunhofer, p++, 110nm SiO_2, channel width 2.5 μm), polymer layer was either spin-coated or laminated onto the substrate. CQD solar cells with device structure of ITO/ZnO/CQD/polymer/MoO_x/Ag were fabricated via layer by layer approach, following previous report.[2]

***Device characterization*:**

Characterization of Solar Cells: Measurement of the current density–voltage (*J*–*V*) characteristics was performed in N_2 atmosphere using a Keithley2400 source unit. A Xenon arc lamp (300 W) served as the light source and the light intensity was calibrated using a filtered Si diode to reduce the spectral mismatch. Solar cell performance was measured using an Air Mass 1.5 G solar simulator with an irradiation intensity of 100 mW cm^{-2}. A shadow mask was used to define device area of 0.049 cm^2 for CQD device and 0.1cm^2 for OPV. The average device parameters were obtained by testing over 30 devices for each type of device. Voltage scan was performed in both forward and backward direction, using step of 10 mV. The EQE measurements were performed in air at zero bias by illuminating the device with monochromatic light supplied from a xenon arc lamp in combination with a dual-grating monochromator. The number of photons incidented on the sample was calculated for each wavelength by using a silicon photodiode.

UPS measurement:

For UPS samples, polymer films were laminated onto a substrate to measure IP of corresponding surface. The UPS measurements were performed with an Omicron SPHERA hemispherical analyzer under He-I excitation (21.22 eV) of an attenuated discharge lamp (Omicron/Focus HIS 13, 1/12 attenuation). The base pressure of the analysis chamber was $8\cdot10^{-10}$ mbar. As substrates, ITO covered glass was used. The samples were prepared in glove box and transferred to the UPS analysis chamber via ambient conditions, estimating the total air exposure time to less than 3 min. The film work functions *(Wf)* are determined from the spectra high binding energy cut-offs via

$$Wf = 21.22eV - E_{HBEC} \tag{1}$$

where E_{HBEC} is the respective cut-off position. The film ionization energies (*IE)* are obtained by adding the photoemission onset originating from the highest occupied molecular orbital states E_{HOMO} w.r.t. to the Fermi level E_{F}:

$$IE = Wf + E_{HOMO} \tag{2}$$

The multi-channeltron detector and analyzer were calibrated to the Fermi edge of a sputter-cleaned Au foil.

GIWAXS:

Grazing Incidence Wide Angle X-ray Scattering (GIWAXS) experiments were conducted at Cornell High Energy Synchrotron Source (CHESS) at D1 beam line. For measurements, incident angle was changed from 0.05 to 0.25. Mathematically, q is equal to $4\pi\sin\theta/\lambda$, where θ denotes total scattering angle multiplied by 0.5 and lamda (λ) is the wavelength of the x-ray used for measurement. The detector used for the measurement is actually a combination of two 100K detectors. All the experiments were conducted in an ambient atmosphere where the relative humidity was around 20-25%.

SCAPS:

Optoelectronic simulations were performed using SCAPS 1D software Simulation parameters (absorption spectra, electron affinities, mobilities and trap densities) for a ZnO/PbS-TBAI/PbS-EDT/electrode architecture were taken from previous work. In short, 10^{16} cm^{-3} trap density in PbS was used, and the electron affinity of PbS was graded from 3.9 to 4.2 eV to reflect the inter-diffusion of ligands between the EDT- and TBAI-treated PbS layers. The model was expanded to include MoO_3 as a metallic contact with deep work function (5.5 eV) and a wide bandgap polymer HTL layer of 10 nm, whose ionization potential was varied from 4.5 to 5.2 eV. The HTL is intrinsic, but if thin enough, it can be remotely doped by the MoO_3contact. Device performance is maximized when the ionization potential of the HTL is matched with that of the shallow PbS-EDT back layer with ionization potential of 4.95 eV.

Device architecture used in simulations.

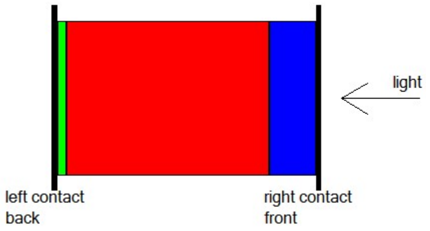

MoO_3 (-5.5 eV) Polymer Graded p-n PbS n-ZnO Ohmic

NEXAFS:

Measured TEY signal was divided by direct beam (measured separately) and normalized to M3 mirror current (measured concurrently). Pre-edge background was fit to Energy^-4, which was extrapolated to full range and subtracted from spectra. Spectra were then normalized at 330 eV. Spectra were fit to edge with peaks, as shown to the right. Orientation analysis was performed on the π^* peak area. as described by Stohr (NEXAFS Spectroscopy, 1992) to determine backbone orientation. π^* peak area should have a $\cos^2$ dependence on incident angle, which can give the azimuthal mean orientation of the orientation distribution

$$I = A * [\frac{P}{3}\left(1 + \frac{1}{2}\{3cos^2\theta - 1\}\{3cos^2\alpha - 1\}\right) + \frac{(1-P)}{2}sin^2\alpha] \qquad (3)$$

where A is constant, P is polarization factor of beamline, θ is incident angle, α is angle of π^* orbital relative o substrate normal. The calculation of dichroic ratio (DR) follows

$$D R = \frac{I(90°) - I(0°)}{I(90°) + I(0°)}. \qquad (4)$$

CMS:

Charge modulation spectroscopy (CMS) was carried out on diodes, fabricated using lightly doped Silicon as the gate, and a 150 nm thermal oxide dielectric. The P3HT surface to be studied was then placed in contact with the dielectric layer. Lastly, 15 nm of semi-transparent gold electrodes thermally evaporated to complete the device. The

CMS spectra were obtained by measuring the changes in infra-red transmission using a Nicolet FT-IR is 50 when 5V and -15V were applied to the MIS device using a Keithley 2400, taking typically 2500 averages. To prevent oxygen degradation, the samples were encapsulated in a nitrogen chamber before being put in FT-IR.

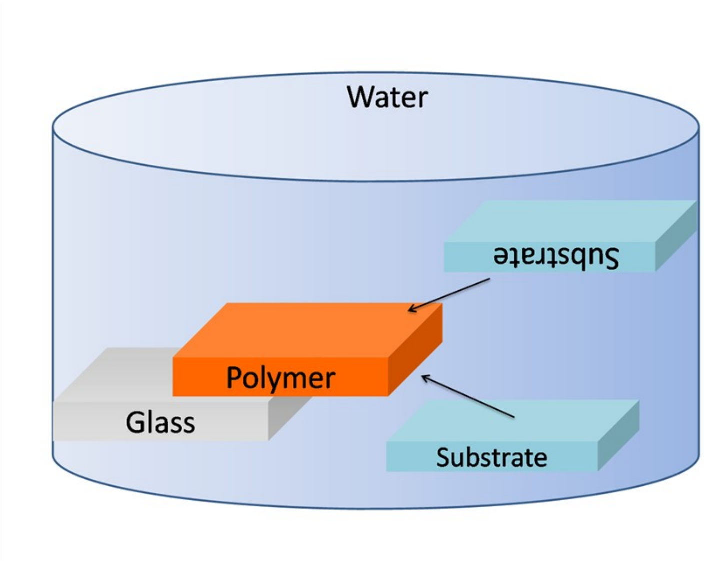

Figure S1. Flipping polymer surfaces by lamination.

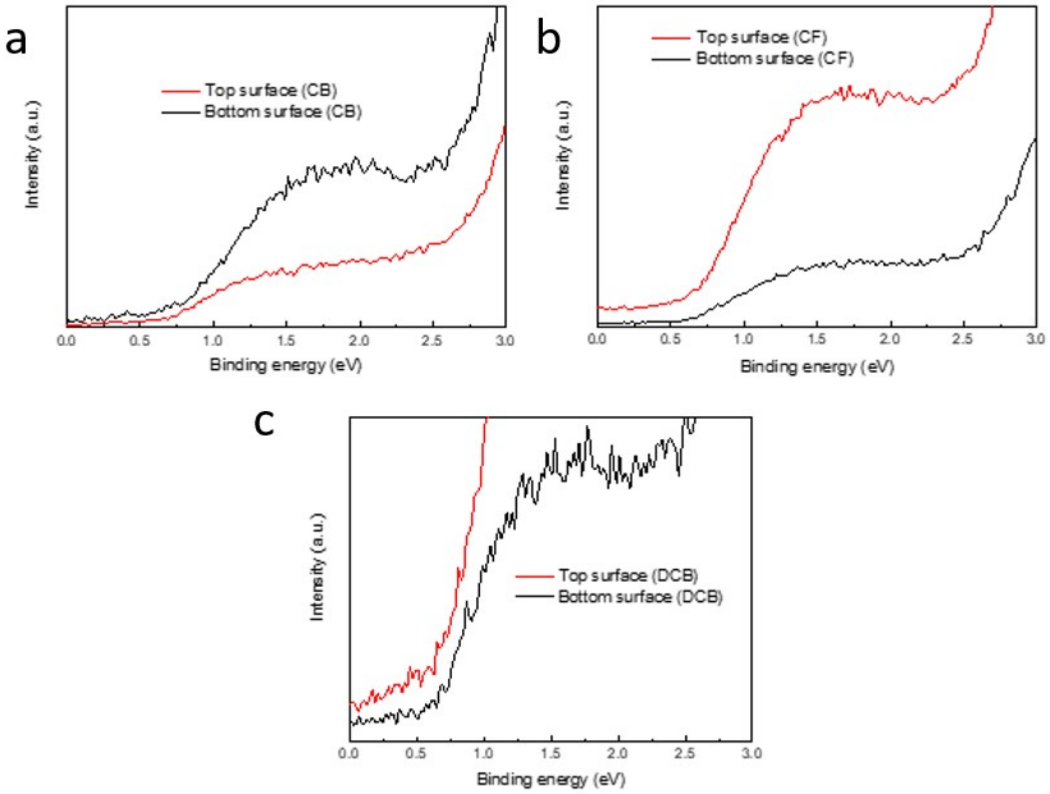

Figure S2. UPS data (HOMO region) of P3HT surfaces processed by (a) chlorobenzene (CB), (b) chloroform (CF) and (c) dichlorobenzene (DCB).

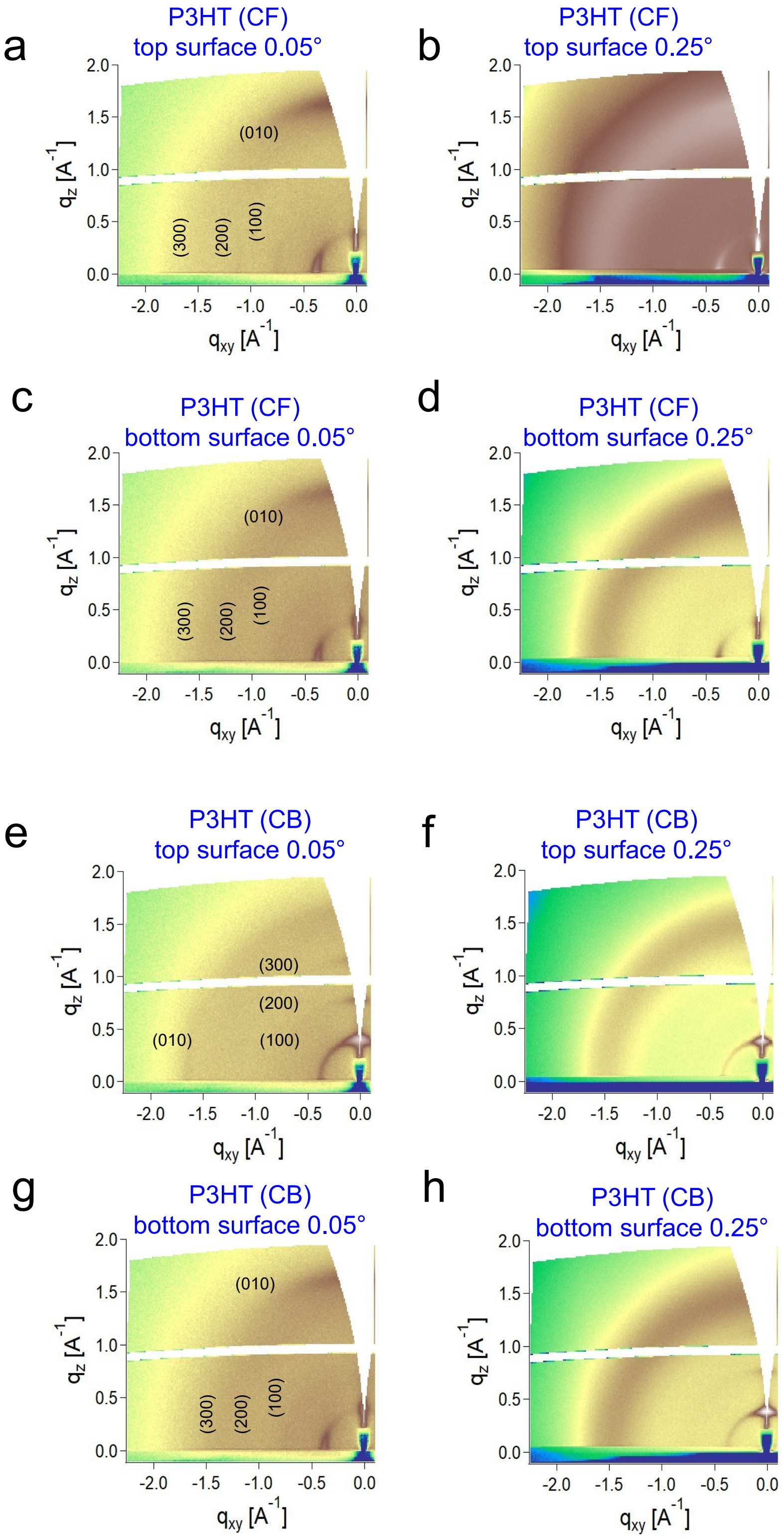

Figure S3. GIWAXS measurements on P3HT top/bottom surfaces with incident angle of 0.05° and 0.25°.

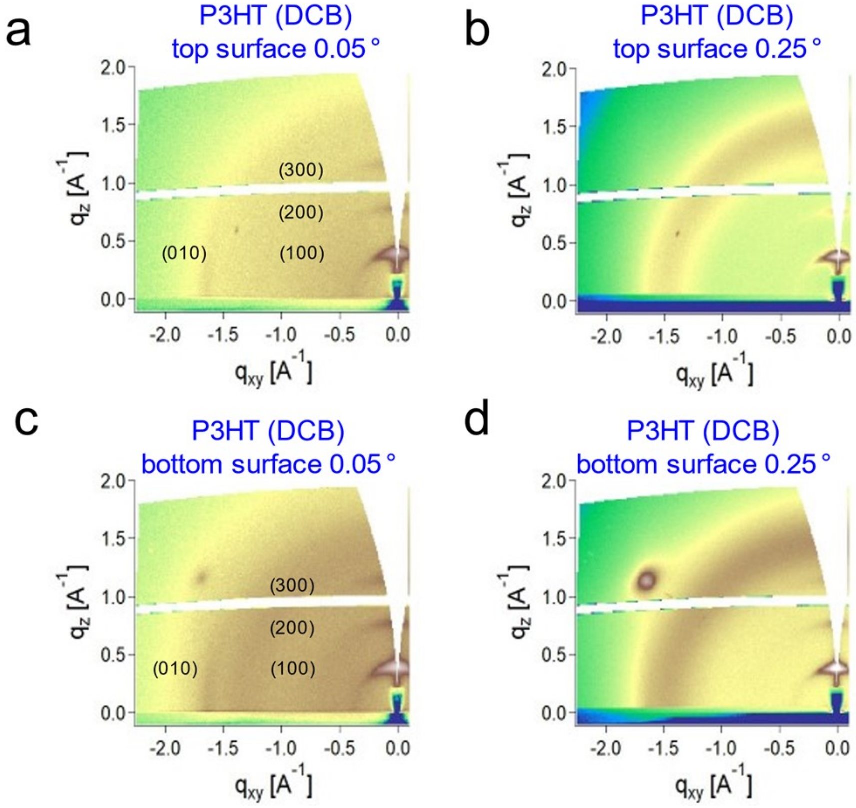

Figure S4. GIWAXS measurements on P3HT top/bottom surfaces with incident angle of 0.05° and 0.25°.

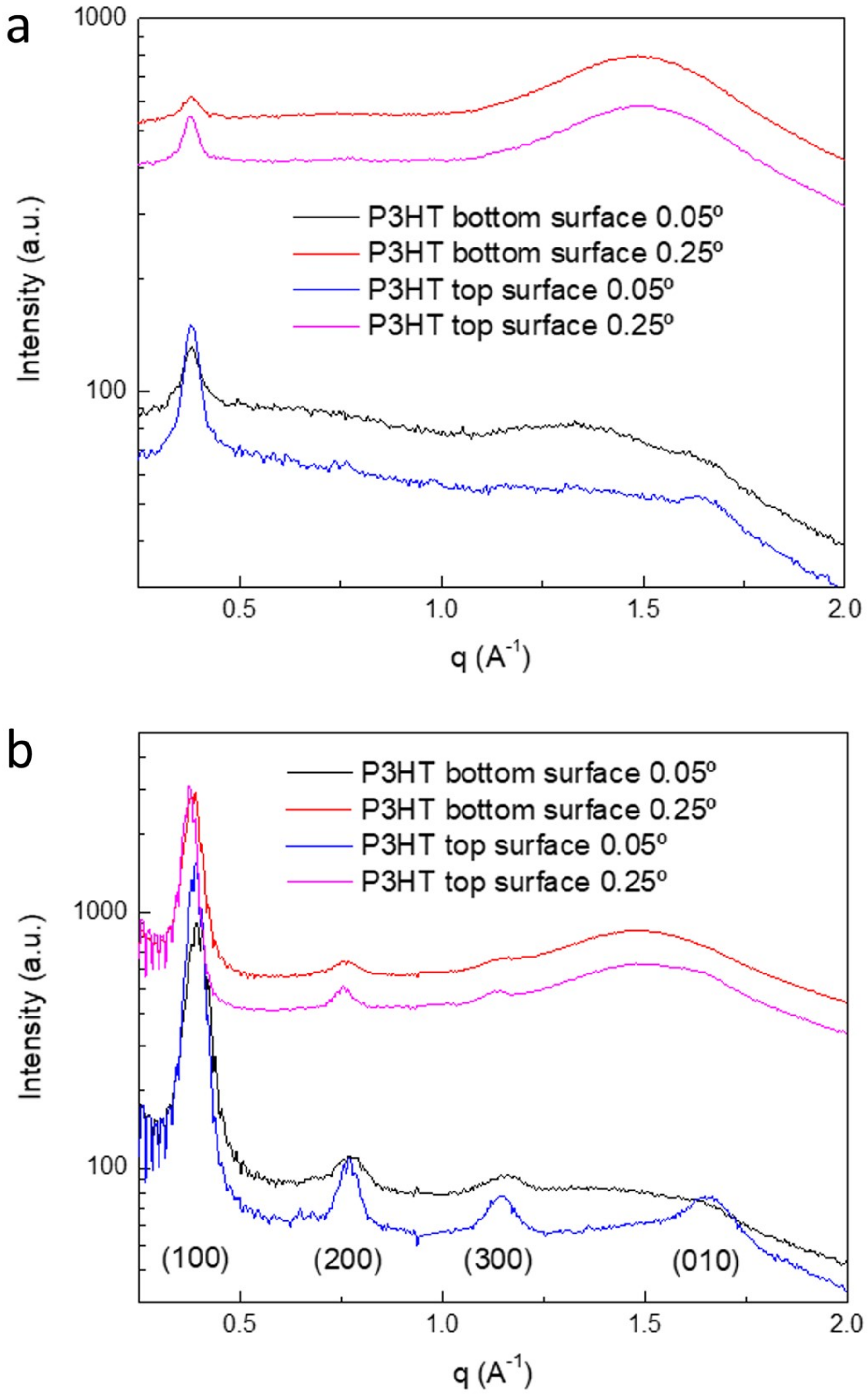

Figure S5. In-plane (m) and out-of-plane sector cut (n) of samples processed by chlorobenzene. Integration of out-of-plane ranges from 80-100°, integration of in-plane ranges from 150-170°.

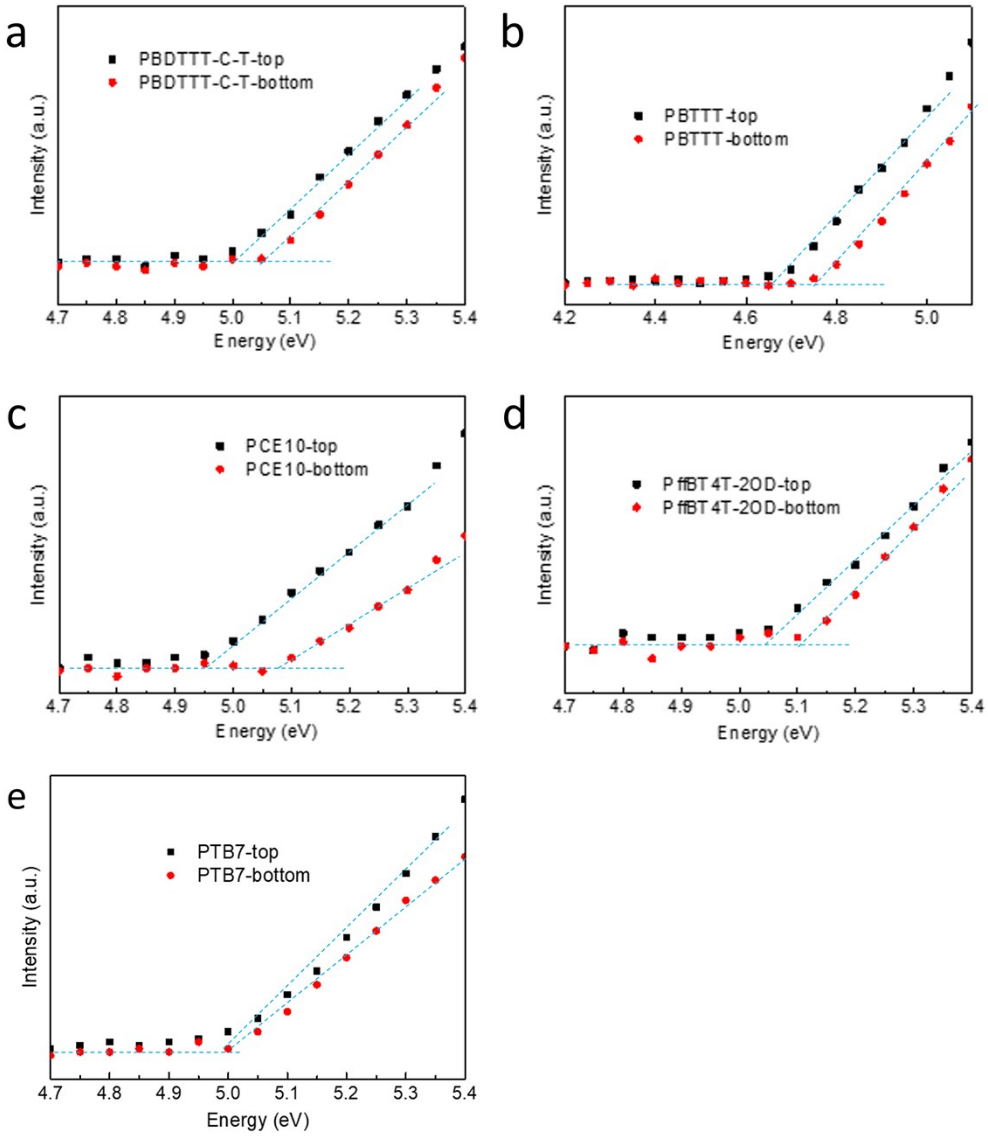

Figure S6. PESA data for different polymer surfaces. The dashed blue lines are fittings to get corresponding IE of surfaces. The average IE values are obtained by measuring three different samples. Additionally, three different sample areas are taken in each measured sample.

Table S1. Figure of merit for P3HT/PCBM bilayer OPVs. P3HT was processed by different solvent and put in contact with PCBM, via top/bottom surface as interface.

Interface	Solvent	V_{OC} (V)	J_{SC} (mA cm^{-2})	FF	PCE (%)
Top	CF	0.32±0.01	2.26±0.18	0.55±0.01	0.5±0.1
Bottom	CF	0.61±0.01	2.33±0.11	0.61±0.02	0.8±0.1
Top	CB	0.31±0.01	1.97±0.22	0.56±0.02	0.4±0.1
Bottom	CB	0.56±0.02	2.01±0.14	0.59±0.03	0.7±0.1
Top	DCB	0.29±0.01	2.29±0.21	0.56±0.02	0.4±0.1
Bottom	DCB	0.44±0.01	2.15±0.12	0.57±0.05	0.5±0.1

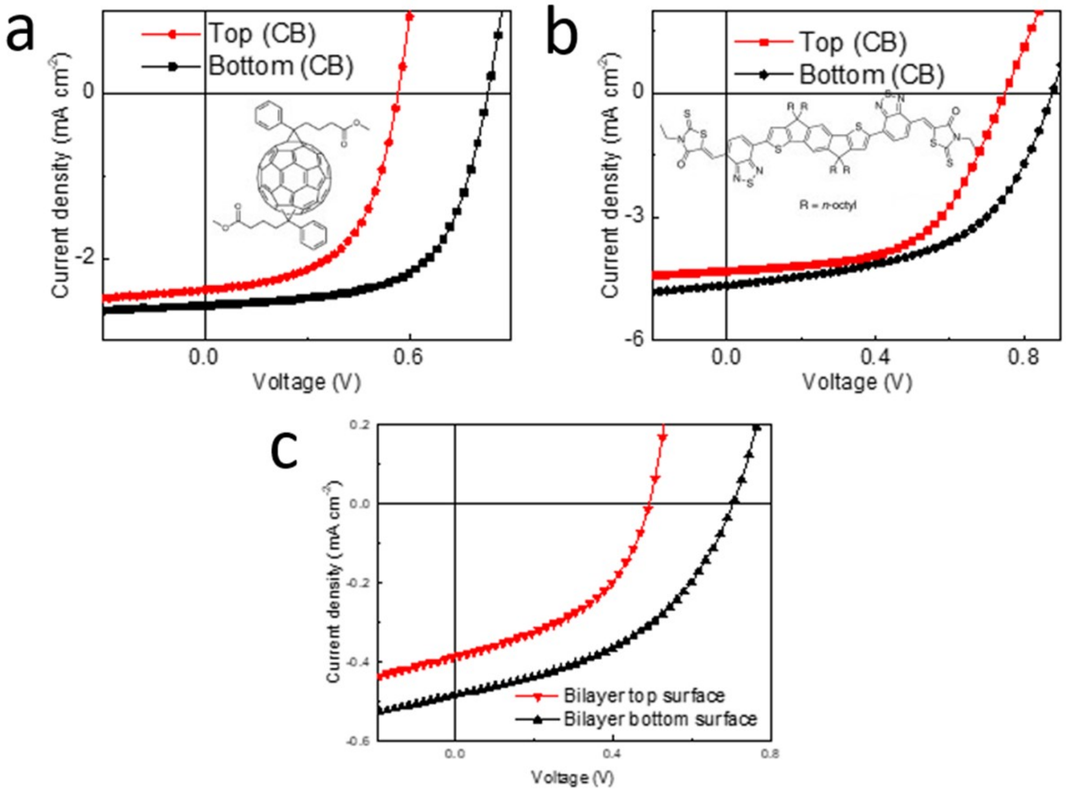

Figure S7. *J*-*V* curves of bilayer OPV using P3HT top/bottom surface as interface with a. Bis-PCBM as acceptor, b. IDTBR and c. ZnO as acceptor, chemical structures are also shown as insertion. Device structure are glass/ITO/ZnO/P3HT/MoOx/Ag or glass/ITO/ZnO/Accptor/P3HT/MoOx/Ag.

We construct D/A interfaces in PHJ devices by using the top/bottom surfaces of P3HT with these acceptors. The *J*-*V* curves are shown in Figure Figure S7 and figures of merit are summarized in Table S3. Similar differences in V_{OC} are observed confirming the different aggregation states of P3HT are responsible for the difference in device performance. We additionally show *J-V* curves of P3HT/ZnO hybrid bilayer photovoltaics in Figure S5 and figure of merit in Table S2. Although possibly with different charge generation mechanism, we can still clearly see the influence of interfacial energetics induced by local ordering of P3HT significantly changes the V_{OC}

of such hybrid device. These results solidify our conclusion that aggregation states of P3HT at the interface dominate the device performance.

Table S2. Figure of merit for P3HT/Bis-PCBM and P3HT/ZnO bilayer devices with different interfaces.

Acceptor	Interface	V_{OC} (V)	J_{SC} (mA cm^{-2})	FF	PCE (%)
Bis-PCBM	Top	0.57±0.01	2.38±0.12	0.56±0.01	0.8±0.1
Bis-PCBM	Bottom	0.83±0.01	2.57±0.14	0.62±0.01	1.3±0.1
O-IDTBR	Top	0.75±0.01	4.31±0.15	0.56±0.02	1.8±0.1
O-IDTBR	Bottom	0.88±0.01	4.65±0.10	0.53±0.01	2.1±0.2
ZnO	Top	0.46±0.02	0.45±0.11	0.41±0.05	0.1±0.01
ZnO	Bottom	0.70±0.01	0.54±0.20	0.43±0.03	0.2±0.01

Table S3. Figure of merit for OPVs. Regio-random P3HT: rra-P3HT, region-regular P3HT: rre-P3HT

Device	Regio-regularity	Annealing °C	Interface	V_{OC} (V)	J_{SC} (mA cm^{-2})	FF	PCE (%)
BHJ	rre-P3HT	150	/	0.60±0.01	8.59±0.18	0.65±0.01	3.3±0.1
BHJ	rre-P3HT	/	/	0.71±0.01	2.25±0.11	0.33±0.02	0.5±0.1
Bilayer	rre-P3HT	150	Bottom	0.68±0.01	8.87±0.14	0.68±0.01	4.2±0.1
Bilayer	rre-P3HT	/	Bottom	0.56±0.02	2.01±0.14	0.59±0.03	0.7±0.1
Bilayer	rra-P3HT	/	Top	0.71±0.01	1.08±0.21	0.34±0.02	0.3±0.1
Bilayer	rra-P3HT	/	Bottom	0.72±0.01	1.08±0.12	0.36±0.05	0.3±0.1

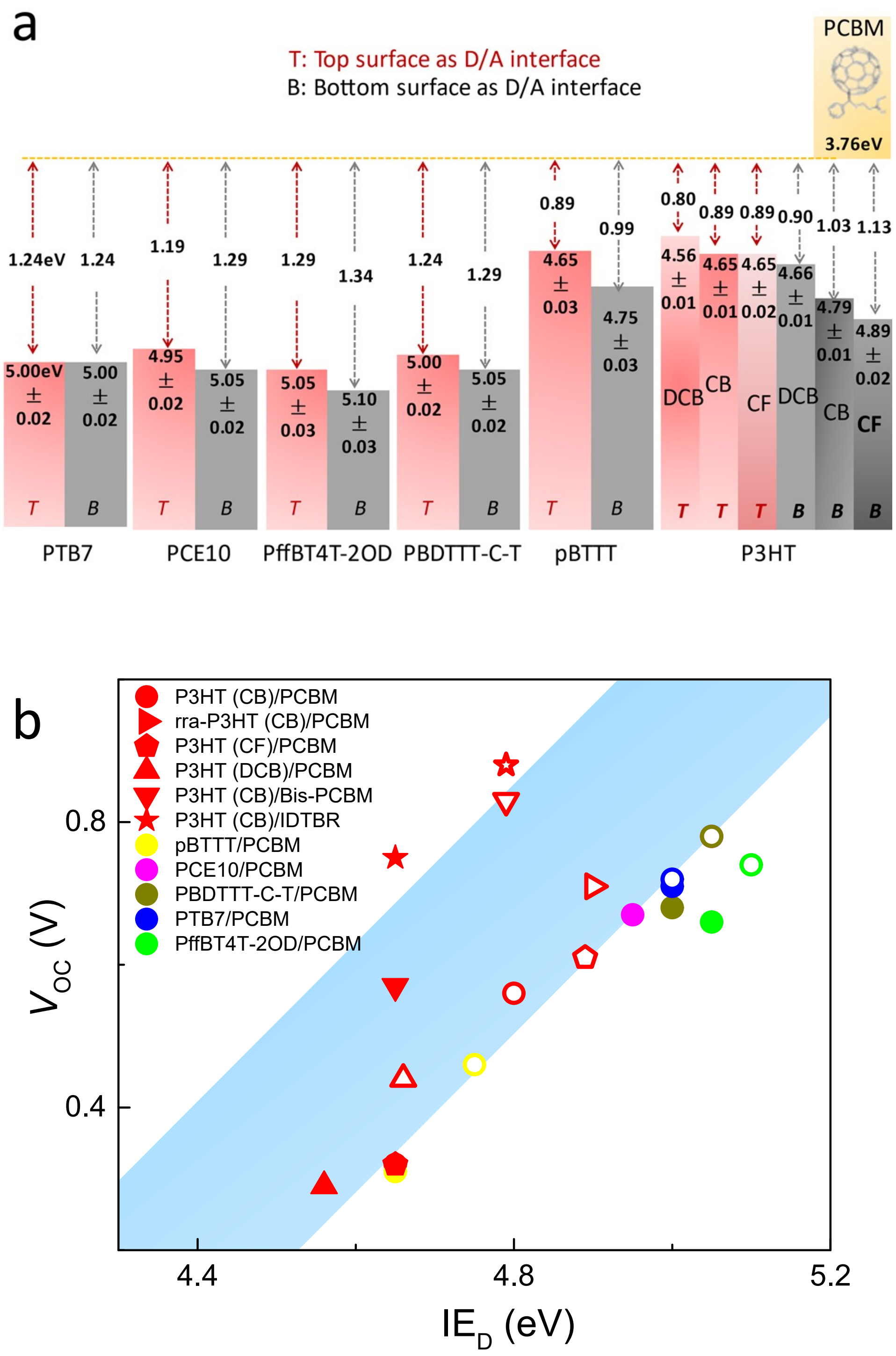

Figure S8. a. Interfacial energetic (unit: eV) of polymer/fullerene bilayers with different polymer surface as interface. b. V_{OC} of bilayer device against the IE of polymer surface used for D/A interface construction. The blue shaded area is the arbitrary shading to indicate a trend.

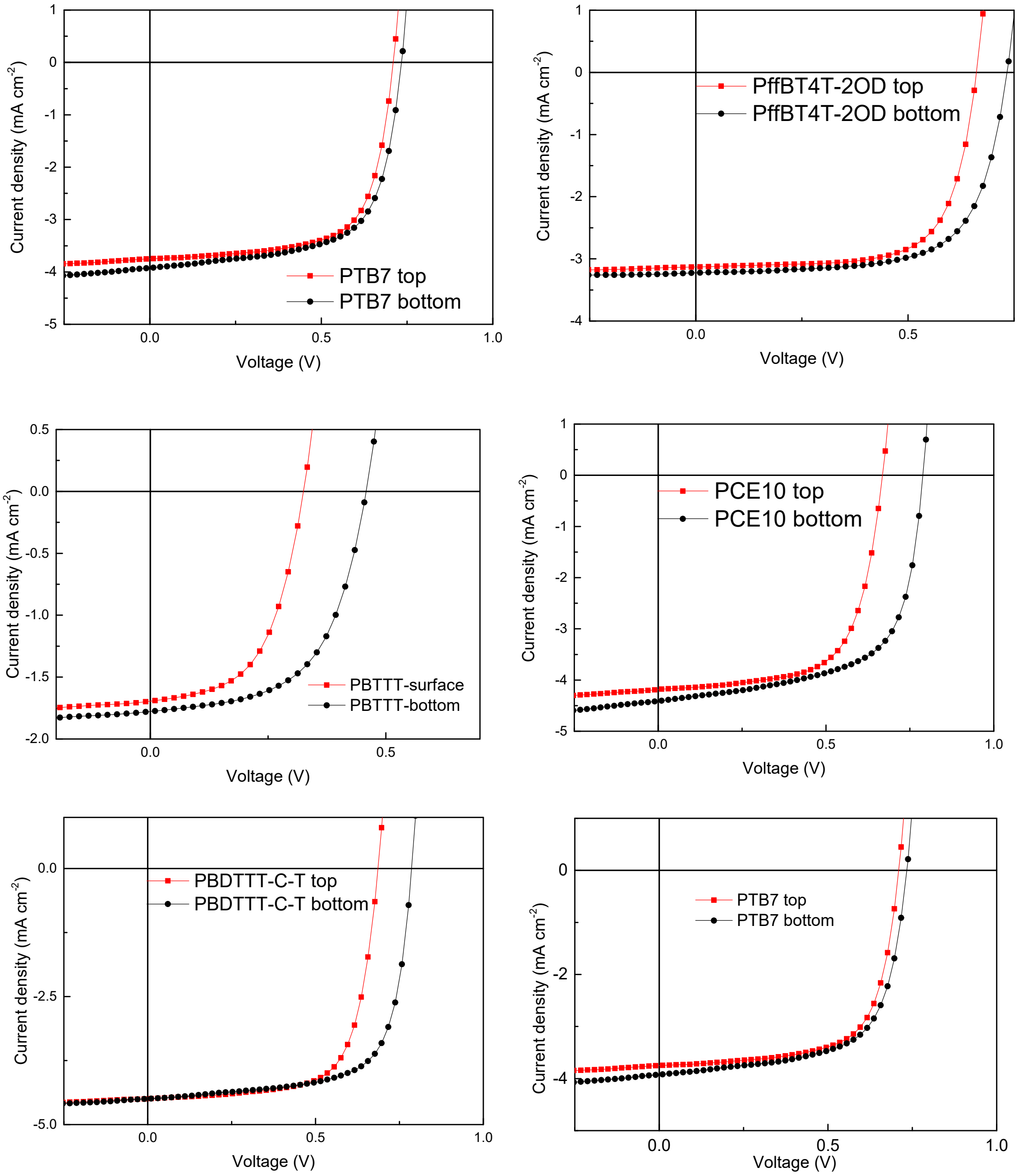

Figure S9. *J*-*V* curves of polymer/fullerene bilayer devices with polymer top/bottom surface as interfaces.

Table S4. Figure of merit for bilayer OPVs.

Polymer	Interface	V_{OC} (V)	J_{SC} (mA cm^{-2})	FF	PCE (%)
PBDTTT-C-T	Top	0.68±0.01	4.42±0.17	0.68±0.01	2.0±0.1
PBDTTT-C-T	Bottom	0.78±0.01	4.49±0.13	0.68±0.02	2.3±0.2
PCE10	Top	0.67±0.01	4.21±0.22	0.66±0.02	1.7±0.1
PCE10	Bottom	0.78±0.01	4.39±0.15	0.65±0.03	2.1±0.2
PBTTT	Top	0.32±0.01	1.68±0.31	0.54±0.02	0.3±0.1
PBTTT	Bottom	0.46±0.01	1.78±0.20	0.54±0.05	0.4±0.1
PffBT4T-2OD	Top	0.66±0.01	3.15±0.21	0.66±0.03	1.3±0.1
PffBT4T-2OD	Bottom	0.74±0.01	3.21±0.11	0.64±0.02	1.4±0.1
PTB7	Top	0.71±0.01	3.70±0.10	0.66±0.02	1.8±0.1
PTB7	Bottom	0.72±0.01	3.81±0.15	0.66±0.01	1.9±0.2

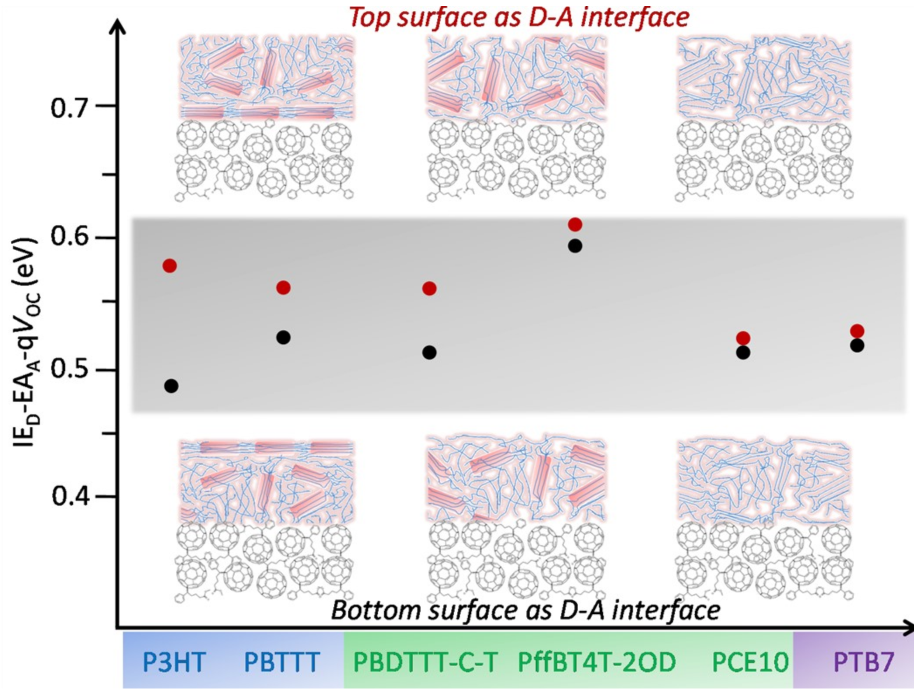

Figure S10. V_{OC} loss (IE_D-EA_A-qV_{OC}) of polymer/PCBM PHJ devices (polymers all processed by CB). The V_{OC} loss gradually diminishes from left to right as we go from more aggregating to least aggregating polymers, indicating this phenomenon is likely associated with order/disorder of the donor polymer at the interface.

Note that due to limited D/A interfacial areas in bilayer device, we are not able to detect or measure E_{CT} by using sensitive EQE since the EQE response in sub-bandgap region is too low. We therefore evaluate the influence of interfacial order on V_{OC}loss, by defining it as IE_D-EA_A-qV_{OC} (shown in Figure S8; red: top surface as interface; black: bottom surface as interface). The data in Figure S8 suggests that when the more disordered buried surface is used the V_{OC} loss is lower by 10 to 90 meV compared to when the ordered top surface is used. This is somewhat counter-intuitive at first glance (disordered interface having lower V_{OC}loss). Because the main focus of this work is to present the different aggregation states in the polymer films instead of searching for the origin of V_{OC} loss in OPV, we here briefly hypothesize two mechanisms to explain the reduced V_{OC}loss in bottom surface based device. The first reason could be associated with energy-gap-law reported recently which essentially identifies a lower (non-radiative) V_{OC} loss in OPV with larger energy of charge transfer state (E_{CT}).[3] We here clearly see a larger interfacial bandgap (IE_D-EA_A) when using bottom surface as interface. Such bandgap has direct impact on determining E_{CT}, thus V_{OC} and the V_{OC}loss in OPV by reducing the coupling between CT state and ground state. We therefore explain the smaller V_{OC}loss by the energy gap law. The second possible mechanism is energy cascade which is widely reported in BHJ devices sweeping out charges from D/A interfaces.[4] Due to different aggregation state in different area of polymer films, we speculate such energy cascade could even exist in pure polymer phase in bilayer OPV. As evidenced by UPS and EQE results in the main text, which probe a depth of 1-2 nm and ~5 nm (exciton diffusion length in bilayer), respectively, show there is different ordering-induced energetics in top/bottom surfaces of the film. This implies a gradient of order through the film with highest order on top surface and lowest order in bottom region, with unknown shape of the gradient. When the disordered bottom surface is used as the interface, charge separation becomes an energetically downhill process. In other words, charges sweep out from D/A interfaces, a process starting from the higher energy disordered interface towards lower energy ordered regions away from the interface. On the other hand, when the top surface is used as interface, it creates the opposite situation whereby a barrier is created for sweeping charges away from the interface, leading to a higher energy loss. The above two explanations are only part of the factors governing V_{OC} and V_{OC}loss in OPVs. Nevertheless, the lower V_{OC}loss observed here certainly offers new insight and potential pathway to reducing energy loss in OPVs, although the definitive mechanism requires further investigation. Other parameters such as aforementioned D/A coupling and charge delocalization can also impact the results here and partially account for the deviation of data from above trend (such as P3HT processed by different solvents). The fact that we obtain higher V_{OC} and lower V_{OC}loss without compromising J_{SC} suggests that selecting/constructing D/A interfaces more judiciously may be promising. Leveraging the stratification approach could be effective at breaking the age-old trade-off between photo-voltage and photo-current in OPV. The current approach does not involve any changes to the device architecture or the choice of materials, but merely to the design of the aggregation state of the dominant D/A interfaces where charge generation occurs and potentially to the energy landscape within the BHJ, while keeping the total absorption of the active layer unchanged.

We note that we here used different way of describing V_{OC}loss in the device by using IE_D–EA_A–qV_{OC}, due to non-measurable E_{CT} in bilayer devices. The reported V_{OC}loss in P3HT:PCBM BHJ device by E_{CT}–qV_{OC} is around 0.6 eV.[5] Such value could be even higher considering the binding energy of CT state when converted into the way we used here.[6] Additionally, the annealing induced “BHJ like” PHJ devices presented above shows 80 meV improvement in terms of V_{OC}. Considering the overall (bulk) bandgap of P3HT in this device is similar compared to that of annealed BHJ device, as evidenced by onset of EQE data, the V_{OC}loss in this device should therefore be reduced by similar amount, leading to an over 4% efficiency. Such results definitely offer a new way of interfacial morphology control to reduce energy loss. Last thing we wish to mention here is rra-P3HT, which possesses V_{OC}loss of 0.43 eV. Such value is slightly lower than that in that in regioregular P3HT devices (0.46 eV as the lowest among different solvents/surfaces). Although complicated factors discussed above are involved here, we again see interfacial energetics dominate V_{OC} and V_{OC}loss (likely due to reduced coupling between CT state and ground state outcompete the impact of localization of charges).

Table S5. V_{OC} of PHJ in this work and corresponding V_{OC} of BHJ reported in literatures.

Donor	Acceptor	Device	Annealing (°C)	Interface used as HJ	PHJ V_{OC} (V)	Reported BHJ V_{OC} (V)
P3HT CF	PCBM	Bilayer	/	Top	0.60±0.01	/
P3HT CF	PCBM	Bilayer	/	Bottom	0.71±0.01	/
P3HT CB	PCBM	Bilayer	/	Top	0.68±0.01	/
P3HT CB	PCBM	Bilayer	/	Bottom	0.56±0.02	/
P3HT CB	PCBM	Bilayer	150	Bottom	0.68±0.01	/
P3HT DCB	PCBM	Bilayer	/	Top	0.56±0.02	/
P3HT DCB	PCBM	Bilayer	/	Bottom	0.72±0.01	/
P3HT	PCBM	BHJ	/	/	0.60±0.01	/
P3HT	PCBM	BHJ	150	/	0.71±0.01	/
rra-P3HT	PCBM	Bilayer	/	Top	0.71±0.01	/
rra-P3HT	PCBM	Bilayer	/	Bottom	0.72±0.01	/
P3HT	Bis-PCBM	Bilayer	/	Top	0.57±0.01	0.73[7]
P3HT	Bis-PCBM	Bilayer	/	Bottom	0.83±0.01	0.73
P3HT	O-IDTBR	Bilayer	/	Top	0.75±0.01	0.72[8]
P3HT	O-IDTBR	Bilayer	/	Bottom	0.88±0.01	0.72
P3HT	ZnO	Bilayer	/	Top	0.46±0.02	/
P3HT	ZnO	Bilayer	/	Bottom	0.70±0.01	/
PBDTTT-C-T	PCBM	Bilayer	/	Top	0.68±0.01	0.75[9]
PBDTTT-C-T	PCBM	Bilayer	/	Bottom	0.78±0.01	0.75
PCE10	PCBM	Bilayer	/	Top	0.67±0.01	0.80[10]
PCE10	PCBM	Bilayer	/	Bottom	0.78±0.01	0.80
PBTTT	PCBM	Bilayer	/	Top	0.32±0.01	0.55[11]
PBTTT	PCBM	Bilayer	/	Bottom	0.46±0.01	0.55
PffBT4T-2OD	PCBM	Bilayer	/	Top	0.66±0.01	0.77[12]
PffBT4T-2OD	PCBM	Bilayer	/	Bottom	0.74±0.01	0.77
PTB7	PCBM	Bilayer	/	Top	0.71±0.01	0.71[13]
PTB7	PCBM	Bilayer	/	Bottom	0.72±0.01	0.71

We see that the V_{OC} of reported BHJs, in most cases, lies in between the value of PHJ using top and bottom surface of polymer as D/A interface. Such results suggest our methodology proposed here can be generally applied to reveal the nature of distributed interfaces within these modern BHJs. In most cases, we observe the BHJ showing a V_{OC} approaching that of the PHJ with the buried interface, which is more disordered. This suggests the charge generation is likely dominated by less ordered sharp interfaces or intermixed domains where molecular coupling is weakened. The V_{OC} of these BHJs could therefore be further improved if interfacial morphology control were available to enable disorder at the interface and increasing order further from the interface in the pure domains. On the other hand, we find BHJs based on pBTTT and PffBT4T-2OD showed V_{OC} higher than the respective PHJs. We ascribe this phenomenon to the likelihood that charge generation is dominated by a lower aggregation or intermolecular coupling interfacial state than achieved in the nominally sharp interfaces in the PHJ devices.

Table S6. Figure of merit for CQD solar cells.

Polymer	Interface	V_{OC} (V)	J_{SC} (mA cm^{-2})	FF	PCE (%)	Interfacial band offset: IP_{CQD}-IP_{P} (eV)
PCE10	Top	0.60±0.01	20.72±0.59	0.37±0.05	4.73±0.47	-0.15
PCE10	Bottom	0.60±0.01	21.57±0.37	0.63±0.01	8.34±0.17	0.05
PTB7	Top	0.61±0.01	22.69±1.01	0.53±0.01	7.93±0.35	-0.10
PTB7	Bottom	0.61±0.01	22.95±0.67	0.53±0.01	7.95±0.24	-0.10
P3HT	Top	0.62±0.01	22.29±0.21	0.62±0.01	8.21±0.20	0.13
P3HT	Bottom	0.63±0.01	23.41±0.11	0.63±0.01	9.80±0.12	0.25

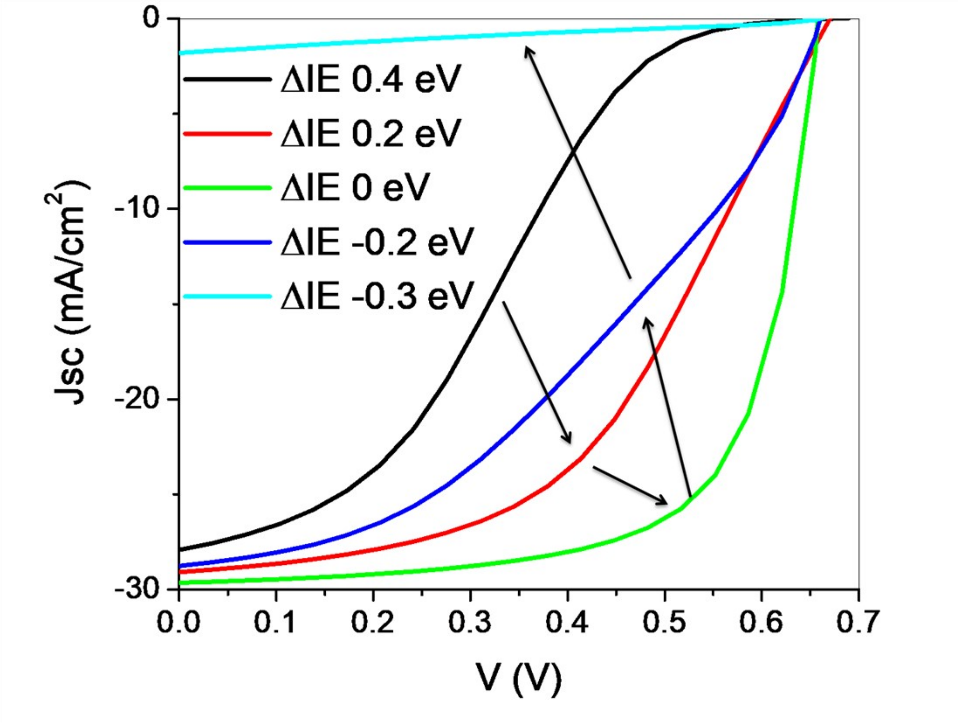

Figure S11. *J*-*V* curves from solar cell capacitance simulator (SCAPS) simulation of different energetic at interfaces (V_{OC} condition)

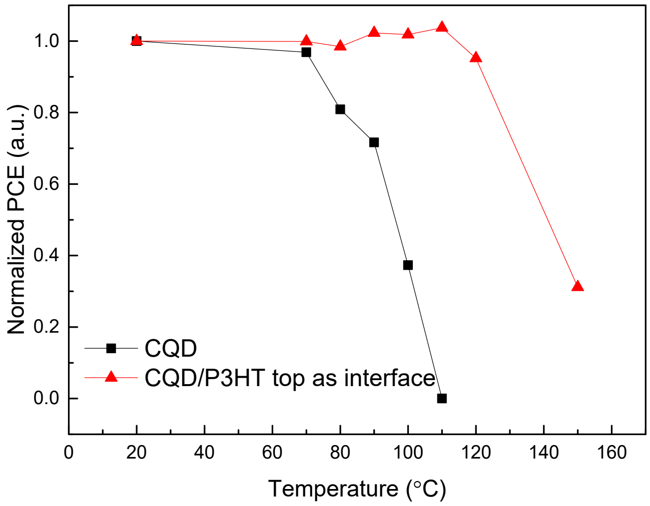

Figure S12. Thermal stability of CQD PV with different charge extraction interfaces (MoO_x/CQD for control device). The devices are heated up at designated temperature for 10 min under dark.

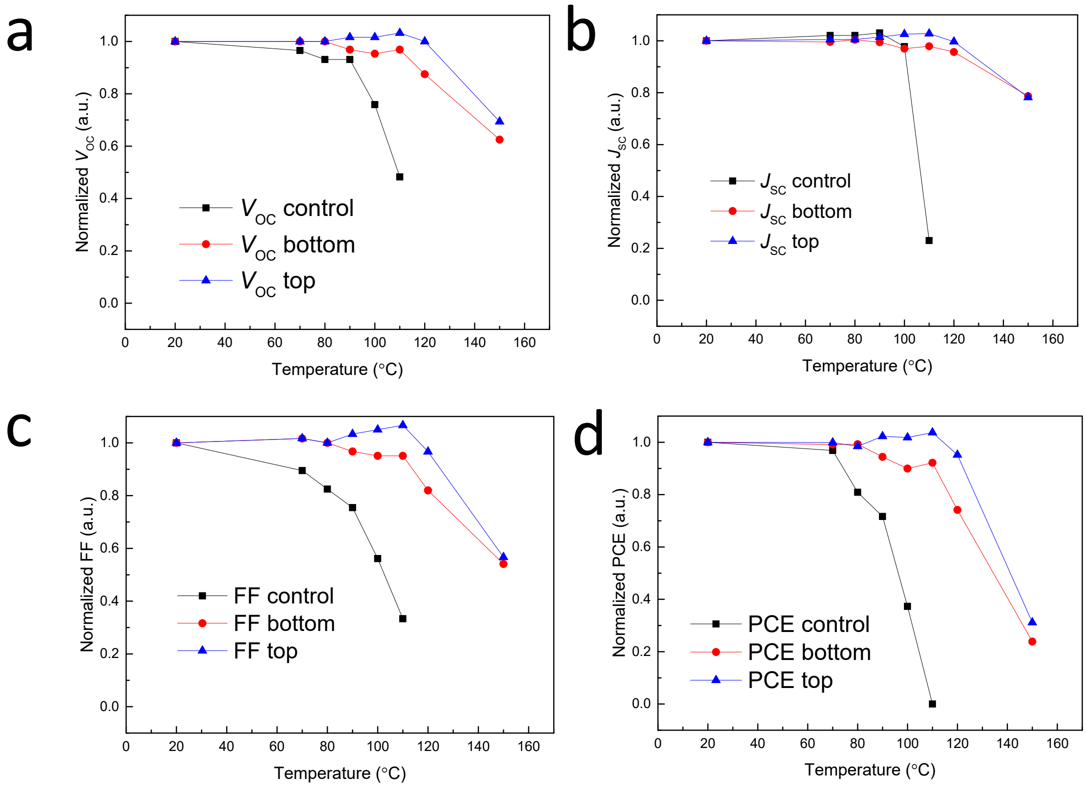

Figure S13. CQD device (with different interface) parameters under different temperatures.

Apart from above routine device characterization, thermal stability has not been carefully explored for CQD PVs, yet is a major goal for industrial compatibility. As a standard, solar cells must be stable at 85°C. We therefore further find the thermal stability is significantly enhanced by polymer film capping atop the CQD absorber. As shown in Figure S10, efficiency of control device starts to drop gradually when temperature is above 70°C and completely killed at 110°C. On the other hand, efficiency of the devices with P3HT as HTL remains stable until 110°C and still functional even at 150°C (Figure S11). Such significant improvement might come from the prevention of degradation from halide ligands of CQD under high temperature. We believe the PCE reduction observed in control solar cells for >70°C is due to detachment of EDT surface ligands at these high temperatures. This likely results in reduction of p-doping in the PbS CQDs forming the HTL. Besides leading to a reduced depletion width in the CQD absorber layer, this also decreases the V_{OC} which is defined by the separation of the quasi-Fermi levels of the ETL and HTL. This is in agreement with the reduced V_{OC} observed for these devices at higher temperatures. By addressing the above concern, P3HT HTL alleviates this performance loss resulting in stable PCEs at temperatures as high as 110°C, making these devices amongst the most thermally stable CQD PV reported to date. Although a mechanistic understanding behind the role of P3HT in improving thermal stability is beyond the scope of this paper, we posit that P3HT acts as a barrier to detachment of the halide ligands from CQD surfaces at high temperatures. This observation has possible explanations in the parallel field of perovskite PV where interlayers are occasionally introduced between the perovskite absorber and the top electrode to suppress ion migration and improve thermal stability.[14, 15]

Reference

1. L. K. Jagadamma, M. Abdelsamie, A. El Labban, E. Aresu, G. O. Ngongang Ndjawa, D. H. Anjum, D. Cha, P. M. Beaujuge and A. Amassian, *J. Mater. Chem. A*, 2014, **2**, 13321-13331.
2. X. Z. Lan, O. Voznyy, A. Kiani, F. P. G. de Arquer, A. S. Abbas, G. H. Kim, M. X. Liu, Z. Y. Yang, G. Walters, J. X. Xu, M. J. Yuan, Z. J. Ning, F. J. Fan, P. Kanjanaboos, I. Kramer, D. Zhitomirsky, P. Lee, A. Perelgut, S. Hoogland and E. H. Sargent, *Adv. Mater.*, 2016, **28**, 299-304.
3. J. Benduhn, K. Tvingstedt, F. Piersimoni, S. Ullbrich, Y. Fan, M. Tropiano, K. A. McGarry, O. Zeika, M. K. Riede, C. J. Douglas, S. Barlow, S. R. Marder, D. Neher, D. Spoltore and K. Vandewal, *Nat. Energy*, 2017, **2**, 17053.
4. A. C. Jakowetz, M. L. Böhm, A. Sadhanala, S. Huettner, A. Rao and R. H. Friend, *Nat. Mater.*, 2017, **16**, 551-557.
5. K. Vandewal, K. Tvingstedt, A. Gadisa, O. Inganäs and J. V. Manca, *Phys. Rev. B*, 2010, **81**, 125204.

6. S. Athanasopoulos, F. Schauer, V. Nádaždy, M. Weiß, F.-J. Kahle, U. Scherf, H. Bässler and A. Köhler, *Adv. Energy Mater.*, 2019, **9**, 1900814.
7. M. Lenes, G.-J. A. H. Wetzelaer, F. B. Kooistra, S. C. Veenstra, J. C. Hummelen and P. W. M. Blom, *Adv. Mater.*, 2008, **20**, 2116-2119.
8. D. Baran, R. S. Ashraf, D. A. Hanifi, M. Abdelsamie, N. Gasparini, J. A. Röhr, S. Holliday, A. Wadsworth, S. Lockett, M. Neophytou, C. J. M. Emmott, J. Nelson, C. J. Brabec, A. Amassian, A. Salleo, T. Kirchartz, J. R. Durrant and I. McCulloch, *Nat. Mater.*, 2017, **16**, 363-369.
9. L. Ye, Y. Jing, X. Guo, H. Sun, S. Zhang, M. Zhang, L. Huo and J. Hou, *J. Phys. Chem. C*, 2013, **117**, 14920-14928.
10. L. Ye, S. Zhang, W. Zhao, H. Yao and J. Hou, *Chem. Mater.*, 2014, **26**, 3603-3605.
11. Q. Sun, K. Park and L. Dai, *J. Phys. Chem. C*, 2009, **113**, 7892-7897.
12. Y. Liu, J. Zhao, Z. Li, C. Mu, W. Ma, H. Hu, K. Jiang, H. Lin, H. Ade and H. Yan, *Nat. Commun.*, 2014, **5**, 5293.
13. Z. He, C. Zhong, X. Huang, W.-Y. Wong, H. Wu, L. Chen, S. Su and Y. Cao, *Adv. Mater.*, 2011, **23**, 4636-4643.
14. G.-W. Kim, H. Choi, M. Kim, J. Lee, S. Y. Son and T. Park, *Adv. Energy Mater.*, 2020, **10**, 1903403.
15. H. D. Pham, T. C.-J. Yang, S. M. Jain, G. J. Wilson and P. Sonar, *Adv. Energy Mater.*, 2020, **10**, 1903326.